Science of the Total Environment 948 (2024) 174895

Contents lists available at ScienceDirect

Science of the Total Environment

journal homepage: www.elsevier.com/locate/scitotenv

Association of rare earth elements with secondary mineral phases formed during alkalinization of acid mine drainage

Dileesha Jayahansani Kotte-Hewa [a,c,*], Delphine Durce [a], Sonia Salah [a], Delphine Vantelon [b], Erik Smolders [c]

[a] Belgian Nuclear Research Centre, SCK CEN, Boeretang 200, Mol 2400, Belgium
[b] LUCIA Beamline, SOLEIL Synchrotron, L'Orme des Merisiers, Départementale 128, 91190 Saint-Aubin, France
[c] KU Leuven, Department of Soil and Water Management, Kasteelpark Arenberg 20, 3001 Heverlee, Belgium

HIGHLIGHTS

- REE are predominantly scavenged between pH 4–6 by Al/Fe phases.
- LA-ICPMS revealed that REE are adsorbed and/or co-precipitated with Al/Fe phases.
- A smaller fraction of REE is scavenged until pH ~4 by association with gypsum.
- Synchrotron-based analysis revealed that La substitutes for Ca in gypsum structure.

GRAPHICAL ABSTRACT

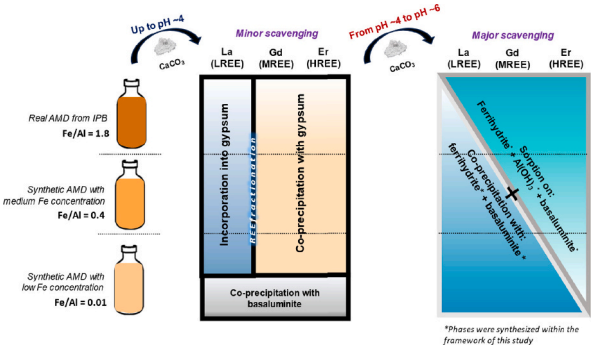

ARTICLE INFO

Editor: Daniel Alessi

Keywords:
Iberian Pyrite Belt (IPB)
Passive treatment systems (PTS)
LA-ICP-MS
Structural incorporation
Co-precipitation
Adsorption

ABSTRACT

Rare Earth Elements (REE) are present in acid mine drainage (AMD) in micromolar concentrations and AMD discharge may lead to an environmental risk. Alkaline Passive Treatment Systems (PTS) are often used to treat AMD and trap toxic trace elements. This study was set up to identify mechanisms by which REE are trapped in or on secondary phases formed in a PTS. Batch alkalinization experiments were performed to simulate PTS by sequentially increasing the pH of AMD collected from the Tharsis mining area inside the Iberian Pyrite Belt and synthetic AMD water samples via $CaCO_3$ addition. The solids that precipitated up to pH ~4 and between pH 4–6 were collected and characterized by Laser Ablation Inductively Coupled Plasma Mass Spectrometry (LA-ICP-MS) in combination with Scanning Electron Microscope/Energy Dispersive X-ray spectroscopy (SEM/EDX) and synchrotron-based X-ray Absorption Spectroscopy (XAS) and synchrotron-based Micro-X-ray Fluorescence (μ-XRF). Results reveal that REE are mostly scavenged between pH 4–6 in association with Al and Fe phases, whereas a smaller fraction is scavenged at pH ~4 by association with gypsum. Synchrotron-based analysis evidences the incorporation of La^{3+} into the gypsum structure by substituting Ca^{2+}, indicating a co-precipitation mechanism with gypsum occurring mainly at low pH. Results from parallel adsorption and co-precipitation tests suggest that the REE scavenging between pH 4–6 could be due to a combination of adsorption and co-precipitation on $Al(OH)_3$ and ferrihydrite. This implies that in PTS, REE would be mainly found in Al- (and

* Corresponding author at: Belgian Nuclear Research Centre, SCK CEN, Boeretang 200, Mol 2400, Belgium.
E-mail address: dileesha.kotte.hewa@sckcen.be (D.J. Kotte-Hewa).

https://doi.org/10.1016/j.scitotenv.2024.174895
Received 7 April 2024; Received in revised form 17 June 2024; Accepted 17 July 2024
Available online 20 July 2024

Fe-) oxyhydroxides occurring in deeper layers of the PTS, i.e., where higher pH-values occur, though a small fraction, especially the light REE, could also be found incorporated into gypsum in the upper layers.

1. Introduction

Rare Earth Elements (REE) include 15 lanthanides in the periodic table plus yttrium. Though the subdivision is not always consistent in the literature (Ayora et al., 2013; Bau et al., 2018; Costis et al., 2021; Ferreira Da Silva et al., 2009; Hassas et al., 2020; Migaszewski and Gałuszka, 2014; Royer-Lavallee et al., 2020), most are classified as Light REE (LREE): from lanthanum (La) to samarium (Sm), Middle REE (MREE): from europium (Eu) to dysprosium (Dy), and Heavy REE (HREE): from holmium (Ho) to lutetium (Lu). Their unique optical, magnetic, and paramagnetic properties have made them indispensable in the production of modern high-technological applications (Ayora et al., 2013; Bau et al., 2018; Costis et al., 2021; Ferreira Da Silva et al., 2009; Hassas et al., 2020; Migaszewski and Gałuszka, 2014; Royer-Lavallee et al., 2020). However, due to the ever-growing, REE are considered as technology critical elements (Ayora et al., 2013; Bau et al., 2018; Costis et al., 2021; Ferreira Da Silva et al., 2009; Hassas et al., 2020; Migaszewski and Gałuszka, 2014; Royer-Lavallee et al., 2020). Today, the primary source of REE are the ore deposits of bastnasite (fluoride carbonate), monazite (phosphate), loparite [(R, Na,Sr, Ca) (Ti, Nb,Ta,Fe^{3+}] and laterite clays (SiO_2, Al_2O_3 and Fe_2O_3) (Costis et al., 2021; London., T.G.S.O, 2011). Those reserves containing REE are mainly located in China (including Bayan Obo), followed by Vietnam, Brazil, Russia, India, Australia (including Mount Weld) and the USA (including Mountain Pass) (London., T.G.S.O, 2011). To secure adequate future supplies for their local industries, most of those countries have been developing policies which, in turn, have raised the concern over future security of supply to the rest of the world (Costis et al., 2021; London., T.G.S.O, 2011) and led researchers to investigate alternative sources (Costis et al., 2021; Ayora et al., 2016; Lozano et al., 2020a; Lozano et al., 2019a; Naidu et al., 2019; Prudencio et al., 2015).

Acid mine drainage (AMD) has been identified as one alternative source for REE (Costis et al., 2021; Ayora et al., 2016; Lozano et al., 2020a; Lozano et al., 2019a; Naidu et al., 2019; Prudencio et al., 2015). In acidic conditions (pH < 3), REE are soluble leading to concentrations several orders of magnitude higher in AMD than in natural water bodies (Ayora et al., 2016; León et al., 2021; Noack et al., 2014; Wang et al., 2021; Zänker et al., 2003). The dispersed alkaline substrate (DAS) passive treatment systems (PTS) installed in the Iberian Pyrite Belt (IPB) for remediating AMD from abandoned mines were shown to significantly scavenge REE (Ayora et al., 2016; León et al., 2021; Cánovas et al., 2020; Rotting et al., 2008). The DAS PTS are mainly based on alkalinization of the AMD through alkaline materials, such as limestone, thereby precipitating the metals (i.e., Fe and Al) as (oxy)hydroxides and oxyhydrosulphates. These systems can raise the pH of AMD waters to about 6.5 (Noack et al., 2014; Akinwekomi et al., 2016). During the alkalinization process, the precipitation of Fe-containing secondary mineral phases identified as schwertmannite ($Fe_8O_8(SO_4)_x(OH)_y$. nH_2O, where x = 1.4–1.5, y = 5.0–5.2) starts between pH 3–4.5 (Lozano et al., 2020b; Bigham et al., 1996; Sánchez-España et al., 2011) and the precipitation of Al-containing secondary mineral phases identified as basaluminite ($Al_4(SO_4)(OH)_{10}.15H_2O$) occurs generally later, i.e. between pH 4.5–6 (Lozano et al., 2020b; Lozano et al., 2019b). In addition, gypsum ($CaSO_4.2H_2O$) may precipitate throughout the complete alkalinization process regardless of the pH (Ferreira Da Silva et al., 2009; Lozano et al., 2020b; Sánchez-España et al., 2011; Lozano et al., 2019b; Bortnikova et al., 2020). The reactions occur inside DAS PTS are given in the supplementary information Table SI 1. Apart from schwertmannite, other Fe phases could also potentially precipitate, such as goethite (α-FeOOH) at pH < 4 (Bigham et al., 1996) or ferrihydrite ($Fe(OH)_3$) at pH ≥ 5.5 (Sánchez-España et al., 2011). Moreover upon ageing low crystalline schwertmannite and ferrihydrite could be transformed to goethite (Sánchez-España et al., 2011). Besides, in addition to basaluminite precipitation, microcrystalline gibbsite or amorphous $Al(OH)_3$ could also possibly form at a pH between 5 and 8 (Sánchez-España et al., 2011).

Removal mechanisms, such as co-precipitation and sorption (i.e., surface complexation) on/with specific precipitated phases are responsible for REE scavenging during AMD alkalinization (Ferreira Da Silva et al., 2009; Lozano et al., 2020b; Lozano et al., 2019b; Ruehl and Hiibel, 2020). Lab-scale column experiments mimicking the DAS technology have shown the absence of REE scavenging with schwertmannite at pH < 4 (Costis et al., 2021; Naidu et al., 2019). Similar studies showed, by using synchrotron-based Micro X-ray Fluorescence (μ-XRF), REE association with basaluminite during AMD alkalinization, suggesting potential sorption and co-precipitation of REE on/with basaluminite (Ayora et al., 2016; Cánovas et al., 2020). The authors further argued sorption to be the most favorable REE scavenging mechanism at a pH close to the formation of basaluminite. In AMD, REE are predominately present as mono-sulfate species (i.e. $REESO_4^+$). Lozano et al. (2019) suggested that REE sorption on basaluminite starts at pH 5 via cation exchange of $REESO_4^+$ with a surface proton to form a monodentate complex. In addition, they suggested REE sorption on schwertmannite to occur through bidentate binding in the pH range of 4.5–6.5 (Lozano et al., 2020b). Other studies suggested the potential association of LREE with gypsum (Ayora et al., 2021; Kotte-Hewa et al., 2023). The authors argued that incorporation of REE into the gypsum structure is possible due to similar ionic radii of LREE in 8-fold coordination and Ca^{2+}. However, a recent study investigating REE partitioning among different precipitated efflorescent sulfates in AMD environments, showed that <20 % of REE were concentrated in gypsum (Ayora et al., 2021). Given the complexity of the secondary phases precipitating/forming, the scavenging of REE during the alkalinization of AMD in PTS could result from various mechanisms. A clear and complete picture of these mechanisms is still missing. The fate of REE is especially unclear in the upper layers of the PTS where pH values <5 are characteristic. Additionally, the impact of the AMD composition and notably of the Fe to Al ratio on REE scavenging was, to our knowledge, never investigated, though the ratio varies from place to place inside IPB. Iron and Al are the most important elements in AMD, and their secondary phase precipitations are believed to be the most important phases trapping/sorbing REE. Detecting REEs at trace concentrations is challenging with conventional solid characterization techniques, which complicates the identification of REE scavenging mechanisms. Hence, employing a 'multi-analysis approach' with cutting-edge techniques is crucial.

The first objective of this study was to identify the minerals hosting REE and the mechanisms involved in REE scavenging during the alkalinization of AMD by calcium carbonate, with special attention to performing the study with environmentally relevant REE concentrations. The second objective was to assess if the Al to Fe ratio in AMD affects REE scavenging and fractionation. Real AMD taken from the IPB and synthetic AMD waters were used and alkalinized, first to pH ~4 and then to pH ~6. The role of Al to Fe ratio was investigated by varying the Fe content of the synthetic AMD waters. The nature of the mineral hosting REE and of the involved mechanism was assessed using a combination of wet chemistry analyses, SEM/EDX, LA-ICP-MS and synchrotron-based Micro X-ray Fluorescence (μ-XRF) and synchrotron-based X-ray Absorption Spectroscopy (XAS). Additional adsorption and co-precipitation tests of REE with relevant mineral phases (i.e., gypsum, schwertmannite, basaluminite, ferrihydrite and $Al(OH)_3$) were performed in parallel to the alkalinization experiments for a better understanding of the REE scavenging mechanisms. For that, the mineral

phases were synthesized in-house.

2. Materials and methods

2.1. Acid mine water samples and characterization

A real AMD sample was collected from a permanent leachate at sulfate dumps inside the Tharsis mining area in the IPB (SW Spain). It will be further referred to as IPB_AMD. The sampling was done at the end of April, representing the intermediate period between wet and dry seasons. During this period higher concentrations of elements (i.e., REE, Al, Fe, and other heavy metals) are present in the AMD. The selection of the AMD sample was not aimed at being fully representative: it was rather selected to provide working conditions with the highest concentration of REE and other elements (i.e., Fe and Al), aiding in the determination of underlying mechanisms. At the point of collection, the sample was filtered through a 0.22 μm PVDF filtration unit. One part of the sample was subsequently acidified using 1 % (*V*/V) HNO_3 (65 % Suprapur, Merck) and kept at 4 °C until analysis by Inductively Coupled Plasma Mass Spectrometry (ICP-MS) (Agilent 7700× ICP-MS) for its elemental composition (Fe, Al, transition metals and REE). Another fraction was kept at 4 °C without acidification for anion analysis using Ion Chromatography, IC (IC Dionex). The composition of IPB_AMD is reported in Table 1.

A low Fe concentration synthetic AMD (0.5 mmol/L) and a medium Fe concentration synthetic AMD (15 mmol/L) were prepared and will be referred to as Syn_LFe and Syn_MFe, respectively. Note that the IPB_AMD corresponds to a high Fe water as compared to the Syn_LFe and Syn_MFe waters. Therefore Fe/Al ratio varies as follows: IPB_AMD > Syn_MFe > Syn_LFe (Table 1). Reagents used to prepare the composition of synthetic AMD waters, along with details on their purity and suppliers, are given in the supplementary information Table SI 2. Both waters have equal Al^{3+} and SO_4 concentrations (see Table 1). The compositions of the synthetic AMDs were defined based on the composition of three samples taken at different points in the Tharsis mine (including IPB_AMD). Sulfate concentrations in both Syn_MFe and Syn_LFe and Fe concentrations in Syn_MFe were defined based on the average concentrations of the Tharsis mine samples. The Fe concentration in Syn_LFe was based on the lowest measured Fe concentration of the Tharsis mine samples. The Al and Mn concentrations in Syn_MFe and Syn_LFe were similar to IPB_AMD. The synthetic waters were spiked with La, Gd, and Er as models for LREE, MREE, and HREE, respectively (details on the spiked solutions are provided in the supplementary information Table SI 2). Higher REE concentrations were added than present in IPB_AMD to ensure their subsequent detection with the solid characterization techniques. No other metal was added to the synthetic AMD waters to avoid interference during characterization/analysis. The pH of the prepared synthetic AMD water samples was measured using an InLab Routine Pro probe (Mettler Toledo). Initial element concentrations of the synthetic AMD waters were measured by ICP-MS after filtration (<0.22 μm using PVDF filters) and acidification using 1 % (*V*/V) HNO_3 (65 % Suprapur, Merck). The concentrations of S in the synthetic AMD waters were measured after filtration (< 0.22 μm using PVDF filters) and acidification using 1 % (V/V) HNO_3 (65 % Suprapur, Merck) by Inductively Coupled Plasma Optical Emission Spectroscopy (ICP-OES; Varian 720ES) and further converted to sulfate concentrations. Initial compositions of Syn_MFe and Syn_LFe are reported in Table 1.

Table 1
The Fe/Al ratio and initial composition of the real AMD sample from the Tharsis mining area in the Iberian Pyrite Belt (IPB_AMD), synthetic medium Fe AMD sample (Syn_MFe), and synthetic low Fe AMD sample (Syn_LFe) (Means and standard deviation; $n = 2$).

	Unit	IPB_AMD	Syn_MFe	Syn_LFe
Fe/Al	n.a.	1.8	0.4	0.01
pH	n.a.	1.8 ± 0.1	1.70 ± 0.02	1.40 ± 0.01
SO_4	mmol/L	400.00 ± 20.00	100.00 ± 0.01	100.00 ± 0.01
Fe		70.0 ± 3.2	15.00 ± 0.18	0.50 ± 0.17
Al		40.0 ± 2.7	34.00 ± 0.28	34.00 ± 0.08
Mn		4.0 ± 0.1	3.00 ± 0.03	3.00 ± 0.01
Cu		1.0 ± 0.6	–	–
Zn		7.0 ± 0.3	–	–
Ca		10.0 ± 0.4	–	–
La	μmol/L	2.0 ± 0.1	6.00 ± 0.01	6.00 ± 0.01
Ce		6.0 ± 0.3	–	–
Pr		0.8 ± 0.3	–	–
Nd		4.0 ± 0.2	–	–
Sm		1.00 ± 0.06	–	–
Eu		0.30 ± 0.02	–	–
Gd		2.0 ± 0.4	5.00 ± 0.01	5.00 ± 0.01
Tb		0.20 ± 0.01	–	–
Dy		1.00 ± 0.07	–	–
Ho		0.20 ± 0.01	–	–
Er		0.70 ± 0.03	5.00 ± 0.01	5.00 ± 0.01
Tm		0.090 ± 0.001	–	–
Yb		0.50 ± 0.03	–	–
Lu		0.07 ± 0.01	–	–

2.2. Batch alkalinization experiments

2.2.1. Sequential alkalinization

Batch sequential alkalinization experiments were conducted with each AMD water (IPB_AMD, Syn_MFe, and Syn_LFe) through the addition of lab based $CaCO_3$ (≥99 % GPR Rectapur, VWR Chemicals) to sequentially increase the pH to pH ~4 and from pH ~4 to ~6 and collect the precipitated solids. These pH-values are considered being representative of Fe- and Al- oxyhydroxysulfates precipitation, respectively. In 250 mL Nalgene tubes, $CaCO_3$ was added to 180 mL of each AMD water to raise the pH to ~4. The amount of $CaCO_3$ added in each AMD is reported in Table SI 3. The suspensions were shaken for two weeks on an orbital shaker (Ohaus Orbital Shaker), and the precipitated solids were separated by centrifugation (Sigma 6-16KS) at 7000 ×*g* for 10 min, recovered, and freeze-dried. The solids precipitated in Syn_MFe, Syn_LFe, and IPB_AMD will be referred to as Syn_MFe_s_pH4, Syn_LFe_s_pH4, and IPB_AMD_s_pH4, respectively. Each supernatant was subsequently filtered by 0.22 μm PVDF filtration units, and the pH was measured using an InLab Routine Pro probe (Mettler Toledo). Samples of 10 mL were taken for further analysis. The filtered supernatants were transferred to cleaned 250 mL Nalgene tubes, and $CaCO_3$ was added to increase the pH to ~6 (Table SI 3). Similar to the previous step, the suspensions were kept in contact for two weeks on an orbital shaker and centrifuged at 7000 ×*g* for 10 min. The supernatants were filtered with 0.22 μm PVDF filtration units, acidified with 1 % (*V*/V) HNO_3 (65 % Suprapur, Merck). The precipitated solids were freeze-dried. The solids precipitated in Syn_MFe, Syn_LFe, and IPB_AMD will be referred to as Syn_MFe_s_pH6, Syn_LFe_s_pH6, and IPB_AMD_s_pH6, respectively.

All supernatants were analyzed by ICP-MS and ICP-OES. The freeze-dried solids were pressed into 1.3 cm-sized pellets for solid characterization by SEM/EDX and LA-ICP-MS.

2.2.1.1. Solid characterization. A Phenom Desktop SEM equipped with an EDX device was used to observe the precipitated solids' morphology and identify their elemental composition. The pellets were mounted on aluminium stubs and coated with an ultrathin layer (5 nm) of gold to make their surfaces conductive. Imaging was done at a voltage of 10 kV, while EDX spot analyses targeting major phases were performed at an elevated voltage of 15 kV.

An Analyte Excite Excimer LA coupled with 8900 Triple Quadrupole ICP-MS was used to determine the association of REE with Fe, Al, Ca, and S in the precipitated solids. La, Gd, and Er were analyzed in Syn_MFe and Syn_LFe solids. In IPB_AMD solids, La, Ce, Pr, and Nd (as representatives of LREE), Gd (as representative of MREE), and Er (as representative of HREE) were analyzed, while the concentration of the other

REE was below the detection limit. A summary of the operational parameters used in the LA-ICP-MS analysis is given in Table SI 4. In total, 13–25 spots per pellet, selected randomly, were analyzed for Fe, Al, Ca, S, and the selected REE. Each spot was ablated and measured every 0.65 s for a 30 s period, and as such ~46 measurements (per element) per spot were obtained. The procedure followed for the calibration of LA-ICP-MS is given in the supplementary information SI.1.

Correlation graphs were plotted by considering the average of the ~46 measurements per spot to obtain spatial correlation (r) between elements. The strength of correlation is defined as follows: $\pm 0.7 \leq r < \pm 1$: Strong correlation; $\pm 0.4 \leq r < \pm 0.7$: Medium/moderate correlation and $\pm 0 < r < \pm 0.4$: Poor/weak correlation (Jackson, 2006).

2.2.2. Direct alkalinization

Another batch alkalinization experiment was conducted in which medium Fe synthetic AMD sample was directly alkalinized to pH ~6 by the addition of 9.2 g/L of $CaCO_3$ with the intention of obtaining solid for synchrotron analysis. Only the medium Fe synthetic AMD sample was used as 1) real AMD sample is too complex regarding elements present and 2) the low Fe synthetic AMD sample is not representative enough of the real AMD sample. The precipitated solid was separated by centrifugation (Sigma 6-16KS) at 7000 ×*g* for 10 min after two weeks of contact time. The supernatant was filtered using a 0.22 μm filtration unit and analyzed by ICP-MS for Fe, Al, Mn, La, Gd, and Er after the addition of 1 % (*V*/V) HNO_3 (65 % Suprapur, Merck) and IC for sulfate without acidification. The recovered solid was freeze-dried and pressed into a 1 cm-sized pellet.

2.2.2.1. Synchrotron-based characterization. The pellet made from the solid precipitated after the direct alkalinization experiment was characterized by synchrotron-based μ-XRF and μ-XAS (XANES+EXAFS) at the LUCIA beamline in SOLEIL Synchrotron facility in France. The former characterization method was used to determine the co-localization of REE with Fe, Al, Ca, and S, while the latter method was used to obtain structural information on REE association mechanism. Based on the energy range used in the LUCIA beamline (0.8–8 keV), it was only possible to determine the La removal mechanism as only the characteristic X-ray absorption energy of La (L_3 line) is within the energy range used in that beamline. La was, in consequence, taken as a reference for LREE. The experimental setup and the details of the data analysis are given in the supplementary information SI.2.

2.3. Batch adsorption and co-precipitation tests

REE adsorption and REE co-precipitation batch tests were performed for a series of relevant minerals that are potential to be precipitated at different pH levels during the alkalinization along the PTS: gypsum, schwertmannite, basaluminite, ferrihydrite and $Al(OH)_3$. These phases were synthesized in the laboratory, following the well-established protocols to differentiate REE removal mechanisms between adsorption, co-precipitation, and structural incorporation to improve insights better. The synthesis of each mineral phase is detailed in the supplementary information SI.3. The REE studied were limited to La (LREE), Gd (MREE) and Er (HREE).

2.3.1. Batch adsorption tests

Batch adsorption tests were carried out with 10 g/L suspensions in duplicates and following a similar procedure as described by Lozano et al. (2020, 2019). Sorption on the synthetized schwertmannite and basaluminite was studied at pH ~4, sorption on ferrihydrite and $Al(OH)_3$ at pH ~6 and sorption on gypsum at both pH-values. A stock solution consisting of 0.6 mmol/L La, 0.5 mmol/L Gd, 0.5 mmol/L Er, and 20 mmol/L SO_4^{2-} was prepared in ultrapure water. High concentrations of REE were used to ensure detection in solution by ICP-MS after sorption. A fraction of the stock solution (initial pH = 2) was adjusted to pH ~4, another to pH ~6, by addition of 1 mol/L NaOH. About 300 mg of the synthetic mineral phase was added to 30 mL of solution, and the suspensions were shaken on an orbital shaker (Ohaus Orbital Shaker) at a constant speed for four days. The suspensions were then centrifuged for 10 min at 4000 ×*g* followed by filtration through 0.22 μm PVDF membrane filter units, and the supernatants were measured by ICP-MS for La, Gd, and Er after acidification with 1 % (*V*/V) HNO_3 (65 % Suprapur, Merck).

2.3.2. Co-precipitation tests

Co-precipitation experiments were performed with gypsum, schwertmannite, basaluminite, and ferrihydrite. La (0.6 mmol/L), Gd (0.5 mmol/L) and Er (0.5 mmol/L) were added during the synthesis of each mineral phase as mentioned under the supplementary information SI.3. The supernatants separated after centrifugation for 10 min at 4000 ×*g* were measured using ICP-MS for La, Gd and Er after acidification with 1 % (*V*/V) HNO_3 (65 % Suprapur, Merck).

3. Results

3.1. Analysis of supernatants after sequential alkalinization

The supernatant compositions of the AMD water samples after the first and the second alkalinization step are shown in Table 2.

During the first alkalinization step, around 23–36 % of the total REE content was scavenged (Table SI 5). There is a clear difference in the scavenging among REE during the first alkalinization step. The LREE were more efficiently removed (24–56 %) than MREE (11–36 %) and HREE (6–19 %) in all three AMDs. Almost all the remaining REE (>99 %) were scavenged during the second alkalinization step (Table SI 5). The highest removal of sulfate, Fe and Al after the first alkalinization step were obtained with the real AMD sample (Table SI 5). Almost all the remaining Fe and Al were removed during the second alkalinization step (Table SI 5). However, only 20 % of the remaining sulfate in the real AMD sample was removed after the second alkalinization step, while 71–73 % of the remaining sulfate in both synthetic AMD samples were removed (Table SI 5).

3.2. Nature of the solids precipitating during alkalinization

3.2.1. SEM/EDX and LA-ICP-MS analysis

The SEM images of the precipitated solids are reported in Fig. 1 and the corresponding EDX spectra are provided in Fig. SI 1. The SEM/EDX results at pH ~4 (Fig. 1.A, .C and .E) revealed that the alkalinization with $CaCO_3$ leads to gypsum precipitation regardless of the pH range and the type of AMD used. The gypsum minerals have a characteristic elongated shape with a length of <30 μm and a width of <10 μm. At pH ~6 (Fig. 1.B, .D, and .F), comparatively wider forms of gypsum minerals with a width of >10 μm have formed. In addition, Fe, O, and S-rich phases with amorphous morphology formed in the solid samples of the real AMD and synthetic medium Fe AMD (Fig. 1.A and .C). Fe-containing phases are visually absent in the synthetic low Fe AMD sample (Fig. 1.E), likely due to low initial Fe concentration (Table 1). However, supernatant analysis showed a decrease in Fe concentration in the corresponding sample (Table 2), indicating some Fe precipitation. Minor amounts of Al (<7 wt% in the real AMD sample and < 20 wt% in the synthetic medium Fe AMD sample) were also identified by EDX in the precipitated Fe-rich phases, revealing that part of Al could have co-precipitated with Fe up to pH ~4. This also agrees with the reduced concentration of Al in the corresponding supernatants (Table 2).

The analysis of supernatants by ICP-MS, indicated the REE removal from the solution (Table 2 and Table SI 5). However, due to the high detection limit of EDX and the complexity of the samples which include the presence of multiple phases and elements leading to overlapping peaks, none of the selected REE could be detected in any of the solids by SEM/EDX, neither at pH ~4 nor at pH ~6.

Table 2
Supernatant compositions of the real AMD sample (IPB_AMD), synthetic medium Fe AMD sample (Syn_MFe), and synthetic low Fe AMD sample (Syn_LFe) after a sequential increase of pH: Concentrations (<0.22 μm) of major and trace elements measured by ICP-MS, SO_4^{2-} after converting measured S by ICP-OES (Means and standard deviations; $n = 2$).

	Unit	After the first step (pH ~4)			After the second step (pH ~6)		
		IPB_AMD	Syn_MFe	Syn_LFe	IPB_AMD	Syn_MFe	Syn_LFe
pH	n.a.	3.90 ± 0.04	3.90 ± 0.01	3.70 ± 0.03	5.9 ± 0.1	5.80 ± 0.01	5.90 ± 0.06
SO_4^{2-}	mmol/L	178 ± 2	62.00 ± 0.06	68.00 ± 0.01	148.0 ± 2.8	17.0 ± 0.3	17.00 ± 0.01
Fe		0.30 ± 0.01	0.30 ± 0.04	0.090 ± 0.001	<LoQ	<LoQ	<LoQ
Al		17.00 ± 0.02	30.0 ± 0.5	32.0 ± 0.3	<LoQ	<LoQ	$(1.0 \pm 0.1) \times 10^{-2}$
Mn		4.00 ± 0.01	3.00 ± 0.01	3.00 ± 0.02	4.00 ± 0.02	3.00 ± 0.02	2.90 ± 0.01
Cu		0.80 ± 0.03	–	–	$(1.0 \pm 0.1) \times 10^{-3}$	–	–
Zn		6.8 ± 0.5	–	–	1.6 ± 0.3	–	–
Ca		14.0 ± 0.1	14.0 ± 0.5	13.0 ± 0.2	11.0 ± 0.1	15.0 ± 0.3	19.0 ± 0.1
La	μmol/L	1.15 ± 0.02	4.8 ± 0.1	4.7 ± 0.1	$(4.0 \pm 0.1) \times 10^{-3}$	$(3.0 \pm 0.1) \times 10^{-2}$	$(4.0 \pm 0.1) \times 10^{-2}$
Ce		2.86 ± 0.04	–	–	<LoQ	–	–
Pr		$(3.80 \pm 0.01) \times 10^{-1}$	–	–	$(7.0 \pm 0.1) \times 10^{-4}$	–	–
Nd		1.89 ± 0.05	–	–	$(3.0 \pm 0.1) \times 10^{-3}$	–	–
Gd		1.04 ± 0.04	4.40 ± 0.14	4.40 ± 0.05	<LoQ	<LoQ	$(9.0 \pm 0.1) \times 10^{-3}$
Er		$(5.40 \pm 0.01) \times 10^{-1}$	4.80 ± 0.25	4.90 ± 0.07	<LoQ	<LoQ	$(2.0 \pm 0.1) \times 10^{-2}$

LoQ: Limit of Quantification.

Element correlations obtained using LA-ICP-MS analysis (Fig. 2) revealed strong correlations ($r > 0.75$) between Ca and S, confirming the presence of gypsum minerals in all the precipitated solids. Notably, the correlations between Ca and S in the solids precipitated during real AMD alkalinization are lower than those obtained during both synthetic AMDs alkalinization (Fig. 2). The LA-ICP-MS results do not confirm the precipitation of Fe—S phases as observed by SEM/EDX as no correlation is detected between Fe and S at pH ~4 (Fig. 2) in any solid. However, the association with Fe and S could be masked by the predominant presence of gypsum. Fe-containing phases are visually absent in the synthetic low Fe AMD sample (Fig. 3.E), likely due to low initial Fe concentration (Table 1). However, the decrease in Fe concentration in the corresponding supernatant (Table 2) indicated some Fe precipitation. Strong correlations obtained between Fe and Al ($r \geq 0.93$) in the precipitated solids of real AMD and synthetic medium Fe AMD samples using LA-ICP-MS further confirmed Al co-precipitation with Fe at pH ~4 (Fig. SI 2). There is a strong correlation ($r = 0.77$) between Al and S in the synthetic low Fe AMD sample (Fig. 2). However, SEM/EDX (Fig. 1.E) did not observe such Al—S phases at pH ~4, probably due to their limited concentration.

At pH ~6, Al, S, and O rich mineral phases formed in the real AMD and synthetic medium Fe AMD samples (Fig. 1.B and Fig. 1.D), while more Al and O-rich phases formed with synthetic low Fe AMD sample (Fig. 1.F). All these phases are clearly amorphous. Furthermore, considerable amounts of Zn were initially present in the real AMD sample and are decreasing upon alkalinization (Table 2). SEM/EDX results revealed favorable co-precipitation of those metals with Al mineral phases (Fig. 1.B).

Similar to what is observed at pH ~4 for Fe and S, no correlation was detected at pH ~ 6 between Al and S using LA-ICP-MS results (Fig. 2), although SEM/EDX analysis revealed Al—S phase precipitation in the real AMD and synthetic medium Fe AMD samples (Fig. 1.B and Fig. 1.D).

3.3. REE association in secondary phases

3.3.1. LA-ICP-MS analysis

The correlations of the selected REE with Ca, S, Fe, and Al calculated from the LA-ICP-MS results are reported in Fig. 3.

At pH ~4, the selected LREE have a strong correlation ($r > 0.83$) with Ca and S in all the solids (Fig. 3.A). In the real AMD sample, the correlation of heavier REE (MREE and HREE) with Ca and S decreases as the atomic number increases with Er showing no correlation. In both synthetic AMD samples, Gd and Er associations with Ca and S are notably stronger ($r > 0.87$) than in the real AMD sample and only slightly lower than for La. The correlation of REE with Fe (Fig. 3.C) and with Al (Fig. 3.E) are moderate to poor in all AMD samples at pH ~4 except in the precipitated solids of synthetic low Fe AMD which show strong correlation with Al (Fig. 3.E). However, the REE concentrations in the supernatants at this pH are similar irrespective of the initial Fe concentration in the synthetic AMD samples (Table 2).

At pH ~6, REE only show a low to medium correlation with Ca and S ($r < 0.63$) in all precipitated solids (Fig. 3.B), even though gypsum precipitation is still present (Fig. 1.B, Fig. 1.D and Fig. 1.F). REE association shifts from gypsum to Al and Fe-containing phases with which moderate to strong correlations are observed in all solids (Fig. 3.D and Fig. 3.F). The association with Al phases is more favoured in both synthetic AMD samples (Fig. 3.F) than in the real AMD sample, which is the opposite for Fe. Supernatant analysis showed that not all Fe precipitated after reaching pH ~4 regardless of the used AMD water (Table 2), and Fe precipitation still occurred in the second alkalinization step. Yet the amount of precipitate was limited, and no Fe phase was detectable by SEM/EDX in the solids collected at pH ~6.

3.3.2. Synchrotron based analysis

Correlation maps obtained from synchrotron based μ-XRF analysis of solids precipitated during the direct alkalinization of synthetic medium Fe AMD to pH ~6 revealed the associations between Ca—S, Ca—La and S—La (Fig. SI 3). However, no correlations were detected between Fe—La and Al—La using this method. The association with gypsum at low pH could mask the association Fe—La and Al—La occurring at higher pH. Furthermore, the analysis of the supernatant indicated a complete removal of La after the direct alkalinization to pH ~6 (Table SI 6).

Based on the μ-XRF results, EXAFS spectra were fitted with the structure of gypsum (crystallographic information file (Project, T.M, 2022)) in which La replaced the central atom (i.e. Ca) without any radius/distance adjustment. Shell-by-shell fitting was followed using the paths generated based on the used gypsum structure. The spectra calculated with FEFF6 yielded the parameters for the paths. Fitting results demonstrated that fitted distances (R) of shells are not off from the reference distances (Fig. 4).

3.4. REE removal after co-precipitation and adsorption

The co-precipitation test results revealed that REE do not co-precipitate with schwertmannite (Table 3). In contrast, REE strongly co-precipitate with ferrihydrite, basaluminite and gypsum in the order ferrihydrite > basaluminite > gypsum (Table 3). La co-precipitates more with gypsum than Gd and Er. The three REE show similar co-precipitation with ferrihydrite and basaluminite (Table 3).

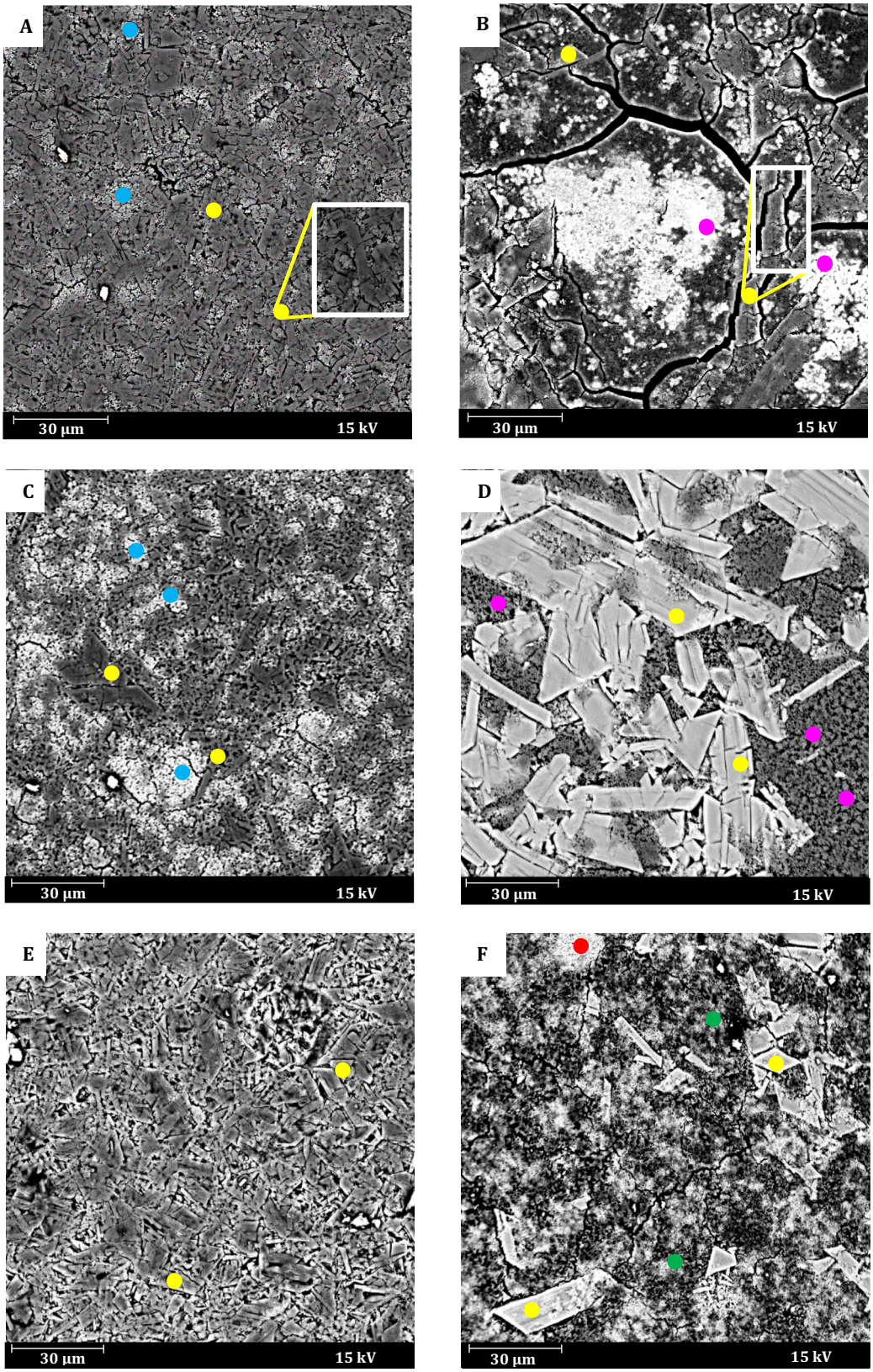

Fig. 1. SEM images of formed solid samples during alkalinization with $CaCO_3$. A: Solids precipitated at pH ~4 with real AMD; B: Solids precipitated at pH ~6 with real AMD; C: Solids precipitated at pH ~4 with synthetic medium Fe AMD; D: Solids precipitated at pH ~6 with synthetic medium Fe AMD; E: Solids precipitated at pH ~4 with synthetic low Fe AMD; F: Solids precipitated at pH ~6 with synthetic low Fe AMD. Yellow dots: Ca, S, and O containing phases (gypsum); Zoomed-in views of selected spots of gypsum are shown inside the white-framed area. Blue dots: Fe, O, and S containing phases with Al-co-precipitation; Pink dots: Al, S, and O containing phases with Cu and Zn co-precipitation. Green dots: Al and O containing phases; Red dot: calcite phase.

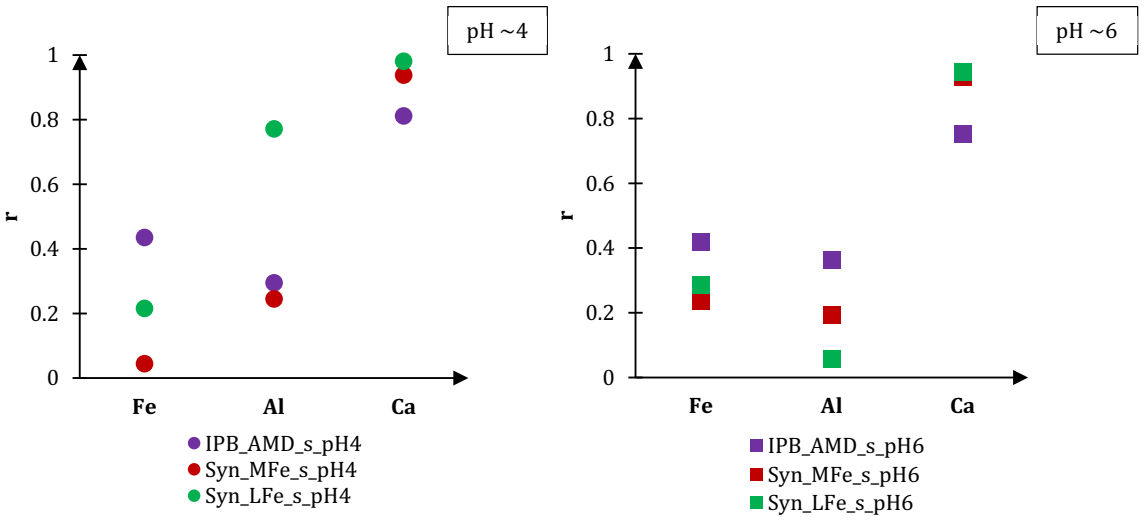

Fig. 2. Fe, Al, and Ca correlation (r) with S in precipitated solids after the first (on the left) and the second (on the right) alkalinization step obtained using LA-ICP-MS data analysis. Purple: the real AMD (IPB_AMD), Red: synthetic medium Fe AMD (Syn_MFe) and Green: synthetic low Fe AMD (Syn_LFe).

Results from the adsorption tests showed that at pH ~4, adsorption of REE on all investigated phases is low with a maximum adsorption of 16 % for Er on basaluminite (Table 4). Adsorption on gypsum at pH ~6 remains low for all REE but adsorption on ferrihydrite is very strong (Table 4). The adsorption on $Al(OH)_3$ at pH ~6 is REE dependent and varies from low for La to strong for Er (Table 4). Adsorption on basaluminite at pH ~6 was not measured here but based on the work of Lozano et al. (2019), it is expected to be strong for all REE.

4. Discussion

4.1. Secondary phase precipitation during alkalinization

It is well established that limestone application to AMD induces gypsum precipitation. Gypsum precipitation is confirmed here as revealed by the SEM/EDX and LA-ICP-MS data (Ayora et al., 2013; Ayora et al., 2016; Kotte-Hewa et al., 2023). The lower correlations between Ca and S measured in the solids precipitated during real AMD alkalinization compared to those precipitated from synthetic AMDs alkalinization suggest that in the field other sulfur or sulphate comprising phases would compete with gypsum precipitation, e.g., Fe—S containing phases. The amorphous nature of precipitated Fe, O and S-rich phases at pH ~4 could indicate the formation of schwertmannite in the real AMD and synthetic medium Fe AMD samples in agreement with previously reported results (Lozano et al., 2020b; Bigham et al., 1996; Sánchez-España et al., 2011).

Precipitation of Al mineral phases is generally favoured at pH > 4.5 (Sánchez-España et al., 2011; Lozano et al., 2020c). However, the analysis of the supernatants sampled at pH ~4 revealed that some Al was removed from the solution in all AMD systems. The strong correlations of Fe—Al in the precipitated solids of real AMD and synthetic medium Fe AMD (Fig. SI 2), and the co-localization of the two elements identified by SEM/EDX (Fig. 1.A and Fig. 1.C) indicate Al co-precipitation with Fe. The medium correlation of Al—S in the precipitated solids of synthetic low Fe AMD indicate the precipitation of an Al—S phase(s), possibly basaluminite. The presence of this phase could not be confirmed by SEM/EDX probably due to its limited amount.

The amorphous nature of Al, S, and O-rich phases observed in the precipitated solids of the real AMD and synthetic medium Fe AMD samples (Fig. 1.B and Fig. 1.D) at pH ~6 could be an indication of basaluminite formation as it is favoured between pH 4.5–6 and was already observed to precipitate in PTS. (Lozano et al., 2020b; Sánchez-España et al., 2011; Lozano et al., 2019b) The precipitation of Al and O rich phases having amorphous morphology in the synthetic low Fe AMD sample indicated precipitation of Al oxides at high pH (~6) (Fig. 1.B). Although, LA-ICP-MS did not exhibit Al—S association (Fig. 2), it still cannot be ruled out that the correlation of S with Al might have been hidden by the gypsum precipitation, which mainly controls the S concentration in the system. Taken together, mainly Fe-S-O-rich phases together with Al co-precipitation dominates at pH ~4 in addition to gypsum up to pH ~4 whereas both Al-S-O and Al—O phases can precipitate at high pH (~6).

4.2. REE immobilization

4.2.1. Nature of the immobilization phases and REE immobilization mechanisms until pH ~4

The REE removal up to pH ~4 is clearly dominated by association with the precipitated gypsum for all AMD waters. The strong correlation between the selected LREE and Ca—S observed in the precipitated solids both by LA-ICP-MS (Fig. 3.A) and μ-XRF (Fig. SI 3) indicates that LREE removal are primarily associated with gypsum. The poor associations of Gd and Er with gypsum in the real AMD sample but being strong in both synthetic AMD samples could be referred to some matrix effects playing in the former sample. Some elements present in the real AMD but absent in the synthetic AMD waters, such as Zn, Cu, and other transition metals (Table 1), may compete with La, Gd, and Er for the co-precipitation/adsorption with/on gypsum during alkalinization. The higher concentrations of REE in synthetic AMD waters as compared to the real AMD water might have also contributed to this difference (Table 1).

The possibility for REE to associate with gypsum has already been mentioned in the literature (Cheong et al., 2022; Dutrizac, 2017; Lin et al., 2019; Sadri et al., 2019; Sadri et al., 2018). Dutrizac (2017), Lin et al. (2019) have suggested that REE incorporation into the gypsum structure could occur by replacing three Ca^{2+} atoms by two REE^{3+} atoms, while Ayora et al. (2021), Sadri et al. (2019), Sadri et al. (2018) suggested REE, especially LREE, incorporation into the gypsum structure by a 1 to 1 calcium replacement due to similar ionic radius of lanthanides with that of Ca^{2+} (Ayora et al., 2021; Sadri et al., 2019; Sadri et al., 2018). The association of LREE and gypsum observed at pH ~4 could thus be attributed to similarities between their ionic radii and the one of Ca^{2+} in the gypsum structure (8-fold coordination) (Ma et al., 2020). The REE (LREE) which are closest to the radius of Ca^{2+} show the highest correlation (r) in the precipitated solids of real AMD sample at pH ≈ 4 (Fig. SI 4). Therefore, the possibility for LREE to be incorporated into the gypsum structure by replacing Ca^{2+} is higher than for MREE and

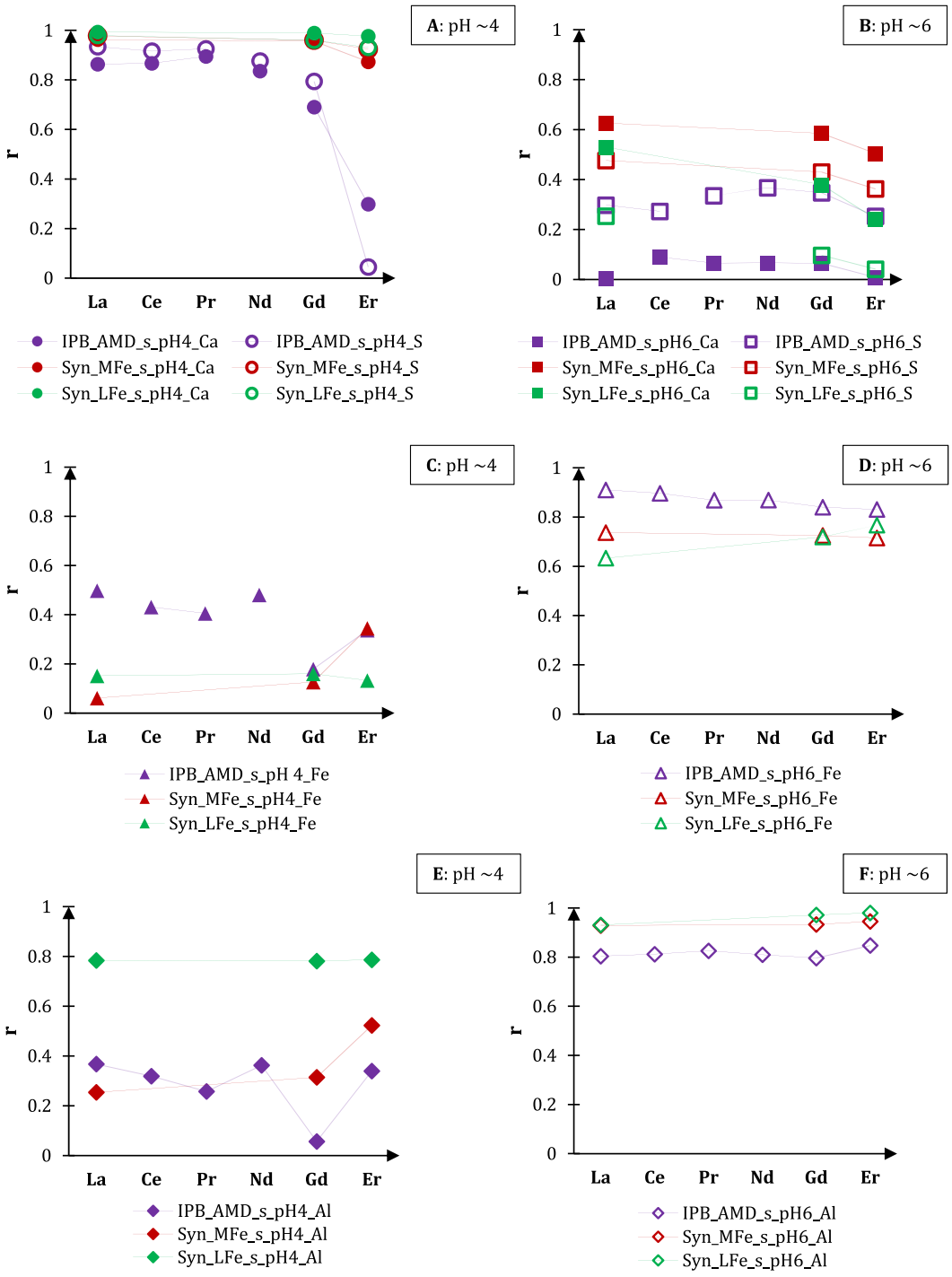

Fig. 3. REE correlation (r) with Ca, S, Fe and Al in precipitated solids after the first (on the left) and the second (on the right) alkalinization step obtained using LA-ICP-MS analysis. A: with Ca and S at pH ~4; B: with Ca and S at pH ~6; C: with Fe at pH ~4; D: with Fe at pH ~6; E: with Al at pH ~4; F: with Al at pH ~6. Purple: real AMD (IPB_AMD), Red: synthetic medium Fe AMD (Syn_MFe) and Green: synthetic low Fe AMD (Syn_LFe).

HREE.

Based on the EXAFS fitting, it can be concluded that one of the mechanisms involved in removing LREE, e.g., La is due to its incorporation into the gypsum structure by replacing the central Ca atom (Fig. 4). Moreover, the observed negligible La, Gd, and Er adsorption on gypsum at pH ~4 and pH ~6 (Table 4) rules out a strong involvement of adsorption as an association mechanism of REE with gypsum. Therefore, the stronger associations between Ca-S-Gd and Ca-S-Er at pH ~4 in both synthetic AMD samples compared to their associations in the real AMD sample (Fig. 3.A) could be resulted from co-precipitation likely in the form of physical entrapment (Harvey, 2000). Co-precipitation with gypsum leads to REE fractionation especially in the real AMD sample, with LREE being preferentially scavenged.

At pH ~4, the correlations of REE with Al are moderate to poor except in the precipitated solids of synthetic low Fe AMD (Fig. 3.E). This synthetic AMD was prepared to favour the formation of Al phases by limiting the concentration of Fe. The Al—S (Fig. 2) and the REE-Al correlations (Fig. 3.E) suggest that REE may be immobilized by co-precipitation with Al—S phase(s), most likely basaluminite. Strong co-precipitation of REE with basaluminite was indeed observed in the co-

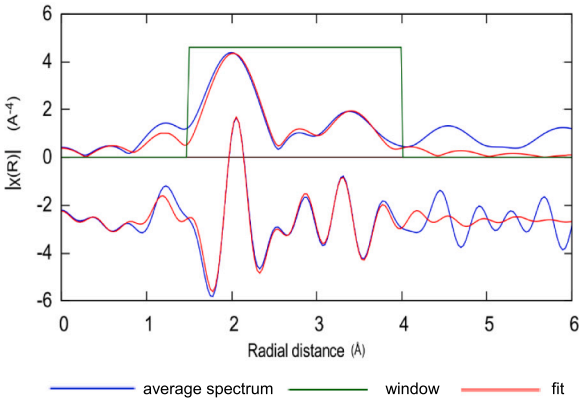

Shell	N	σ^2	R, Å
La-O	8	0.008	2.57
La-MS_2	4	0.003	3.97
La-S_1	2	0.008	3.11
La-S_2	2	0.008	3.66
La-Ca	2	0.001	3.82

Fig. 4. The best fit results obtained by fitting in R space using gypsum structure (cif file (Project, T.M, 2022)) after substituting central Ca atom by La (Artemis software). The blue line represents the measured data and the red line represents the fit. (the amplitude reduction factor, S_0^2, = 0.78, the energy shift parameter = 9.5 eV; N: Coordination number, this was set in agreement with the values provided by the gypsum structure; σ^2: Debye-Waller factor; R: Fitted distance in Angstrom, the multiple scattering path (MS) used is an obtuse triangle La-O-S-La EFF6 mentioned as representing >33 % of the total spectrum, the figure of merite, R_factor = 0.012).

Table 3
% removal of La, Gd, and Er after co-precipitation with mineral phases (means and standard deviations; $n = 2$).

	% removal		
	La	Gd	Er
With schwertmannite	0 ± 0.02	0.6 ± 0.01	0.6 ± 0.01
With ferrihydrite	100 ± 0.01	100 ± 0.01	100 ± 0.01
With basaluminite	88 ± 0.004	89 ± 0.005	89 ± 0.003
With gypsum	83 ± 0.03	75 ± 0.02	60 ± 0.02

Table 4
% removal of La, Gd, and Er after adsorption onto mineral phases at the solid to liquid ratio of 10 g/L (means and standard deviations; n = 2).

Adsorbent	Initial pH	Final pH	% removal		
			La	Gd	Er
Gypsum	4.08 ± 0.10	4 ± 0.02	0 ± 0.03	2 ± 0.07	4 ± 0.06
Schwertmannite		3 ± 0.1	4 ± 0.01	0 ± 0.01	0 ± 0.02
Basaluminite		4 ± 0.2	0 ± 0.02	3 ± 0.01	16 ± 0.01
Gypsum	6.01 ± 0.12	6 ± 0.25	0 ± 0.01	0 ± 0.03	2 ± 0.01
Ferrihydrite		6.4 ± 0.1	92 ± 0.01	98 ± 0.01	100 ± 0.01
$Al(OH)_3$		6 ± 0.19	23 ± 0.01	81 ± 0.01	95 ± 0.01

precipitation tests (Table 3). The presence of higher concentrations of Fe in synthetic medium Fe AMD sample and in the real AMD sample appears to hinder the precipitation of this Al-phase. Yet, the concentrations of REE in the supernatant at pH ~4 are similar regardless of the synthetic AMD type used (Table 2). This indicates that the amount of REE co-precipitated with the Al—S phase in synthetic low Fe AMD is small or that REE co-precipitation with Al—S phase compete so that the total amount of co-precipitated REE remains the same.

At pH ~4, REE do not correlate with Fe in any sample (Fig. 3.C) and REE concentrations in the supernatants are similar irrespective of the Fe concentration in the synthetic AMD waters (Table 2). This reveals that Fe-S-O phase precipitation, schwertmannite, as suggested by SEM/EDX, does not play a significant role in the removal of REE. This agrees well with the results of the co-precipitation tests, which showed no co-precipitation of REE with schwertmannite (Table 3). Taken together, REE removal from AMD waters until pH ~4 is mainly controlled by association with gypsum besides some co-precipitation with basaluminite when the Fe concentration is low.

4.2.2. Nature of the immobilization phases and REE immobilization mechanisms from pH ~4 to pH ~6

REE association shifts from gypsum to Al and Fe-containing phases at pH ~6 with association to Al being more favoured than to Fe (Fig. 3.F and Fig. 3.D). The precipitation of Al is favoured in both the synthetic AMD samples while the precipitation of Fe is favoured in the real AMD sample (Table 2). The more favoured associations with Al at pH ~6 can be attributed to the higher amount of Al (−phases) precipitated in both synthetic AMD samples than in the real sample (Table 2). The substantial removal of REE in this pH range can be attributed to the association with Al phases (e.g. $Al(OH)_3$ and basaluminite) (Table 3 and Table 4) rather than with Fe phases, as most of the Fe precipitated during the first alkalinization step. These results are consistent with the previously reported REE association with Al (Ayora et al., 2016; Cánovas et al., 2020). According to literature, the most dominant Fe phase that would precipitate during sulfate-rich AMD alkalinization above pH 5.5 would be, Fe-oxyhydroxides (i.e., ferrihydrite) (Lozano et al., 2020a; Lozano et al., 2019a; Lozano et al., 2020b; Sánchez-España et al., 2011). While no REE association was evidenced with schwertmannite at pH ~4, the strong REE-Fe correlation observed at pH ~6 suggests an association of REE with Fe-oxyhydroxides either via adsorption or co-precipitation. Hence between pH 4–6, REE removal from AMD water depends on the Fe concentration. Removal by association with ferrihydrite is favoured in Fe-rich AMD waters while removal by Al-rich phases, either basaluminite or gibbsite would dominate in AMD with a high Al—Fe concentration ratio.

The co-precipitation test results revealed the possibility for REE to co-precipitate with basaluminite and ferrihydrite. Yet, it is unlikely that this co-precipitation involves a REE incorporation into the structure of the precipitated Al- and Fe- phases. The Fe^{3+} and Al^{3+} cations are most frequently found in 6-fold coordination (i.e. in ferrihydrite ($Fe(OH)_3$), in goethite (α-FeOOH) and in gibbsite ($Al(OH)_3$)) (Sanchez et al., 2017; Doyle et al., 1999). The differences in ionic radii between REE^{3+} (ranging from 1.16 Å to 0.977 Å) and Al^{3+} (=0.535 Å) or Fe^{3+} (=0.645 Å) in 6-fold coordination are too large, preventing a possible REE^{3+} incorporation. The strong co-precipitation measured could therefore more result from a physical entrapment (Table 3) (Harvey, 2000).

Besides co-precipitation, adsorption is also expected to play a role in REE removal at pH >4.5. Consistent with the absence of a correlation of REE with Ca—S, the adsorption of REE on gypsum at pH ~6 was found negligeable (Table 4). Yet, adsorption of REE on ferrihydrite was strong. Though lower than on ferrihydrite, adsorption on $Al(OH)_3$ was also significant for Er and Gd but low for La. This is consistent with the lower removal of La than Er and Gd observed between pH 4–6 (Table 4).

Adsorption of REE was also observed on basaluminite at pH >5 (Lozano et al., 2019b). The experimental results therefore indicate that the mechanisms involved in removing La, Gd, and Er between pH 4–6 during AMD alkalinization would be adsorption onto and co-precipitation with Al (i.e., $Al(OH)_3$, basaluminite) and Fe (i.e., ferrihydrite) phases. The majority of REE is scavenged in this pH range (Table 2 and Table SI 5); therefore, adsorption and co-precipitation on/with Al phases and, to a lower extent, on/with Fe phases, are the primary mechanisms through which REE get scavenged in PTS. This agrees with the previously reported selective retention of REE in the Al-rich zone (i.e., basaluminite precipitates) inside the limestone-DAS system in Mine Esperanza (Ayora et al., 2016).

Results from this study significantly contributed to obtaining a clear picture of the processes occurring during AMD alkalinization and, most importantly, provided a comprehensive overview of the mechanisms involved in immobilizing REE at various pH levels during alkalinization.

4.3. Policy implications

The near-complete removal of REE (~100 %) using $CaCO_3$ during AMD alkalinization in PTS suggest that REE become concentrated in the precipitated solids overtime, ultimately leading to their disposal in landfills. However, challenges arise at this stage due to the lack of recommended maximum threshold limits for REE in water and soil. While such limits do not currently exist, elevated levels of REE in precipitated solids could pose toxicity risks if released into the environment. Mining effected areas has been shown to have extremely high-risk characterization ratio (i.e. 2606 (Lachaux et al., 2022)), indicating severe risks to exposed freshwater systems. This underscores the urgent need for policy development regarding REE regulation.

If future policies require certain concentration levels for REE in surface discharge, the findings from our research would be helpful for designing remediation systems for REE not only for AMD but also for other scenarios (i.e. phospogypusm waste treatment). This highlights the broader applicability of our research in addressing REE contamination issues beyond the context of AMD.

5. Conclusions

This study focused on identifying the scavenging mechanisms occurring during AMD alkalinization via $CaCO_3$ addition and leading to the immobilization of REE. Both real and synthetic AMDs were used to model complex and simplified systems to perform batch alkalinization, employing high-level characterization techniques such as synchrotron-based methods and LA-ICP-MS to determine the involved mechanisms. The obtained results lead to an improved understanding of the mechanisms responsible for REE immobilization along the PTS at various pH levels.

The immobilization of REE during AMD alkalinization using $CaCO_3$ was identified to involved three different mechanisms occurring simultaneously or at different pH levels: 1) incorporation into the secondary mineral structures, 2) adsorption onto the secondary phases, and 3) co-precipitation with the secondary phases.

Co-precipitation with gypsum immobilizes REE at low pH (<4) by structural incorporation of LREE and to a lower extent by co-precipitation of MREE and HREE. This mechanism leads to a minor removal of REE ranging from 24 to 56 %, (11–36 %) and (6–19 %) for LREE, MREE and HREE, respectively. The resulting REE fractionation would result in a higher mobility of MREE and HREE to the deeper layers of the PTS in comparison to LREE. At high Al/Fe ratio, Al—S phases (e.g., basaluminite) would also contribute to REE immobilization, most likely via co-precipitation confirming the effect from its ratio on REE scavenging.

At higher pH (>4), both Al and Fe phases play a significant role in REE immobilization via combined adsorption and co-precipitation mechanisms. The co-precipitation and adsorption experiments suggest that REE adsorb onto $Al(OH)_3$ and ferrihydrite, co-precipitate with basaluminite and ferrihydrite. These mechanisms lead to a complete removal of the REE from the solution.

The findings suggest fractionation of REE at different depths of the PTS, with LREE more prevalent in the upper layers (pH < 4) due to co-precipitation with gypsum and the remaining REE concentrated in deeper layers (pH > 4) associated to Al and Fe phases. Recovery of REE from PTS may be feasible by targeting deeper layers with higher pH, especially where Al phases precipitate. Geochemical modelling will further elucidate the processes occurring during alkalinization and support the interpretation of the experimental results.

The conclusions made here were drawn from lab-scale experiments and with the use of partly simplified systems, synthetic AMD and pure $CaCO_3$. Further investigations would therefore be needed to determine whether the identified mechanisms are transferable to real PTS systems, where factors such as kinetics (i.e., flow rates, residence time) and ageing (prolonged reaction times) may play a role.

CRediT authorship contribution statement

Dileesha Jayahansani Kotte-Hewa: Writing – original draft, Visualization, Validation, Methodology, Investigation, Formal analysis, Data curation, Conceptualization. **Sonia Salah:** Writing – review & editing, Supervision, Project administration, Methodology, Funding acquisition, Conceptualization. **Delphine Vantelon:** Writing – review & editing, Supervision, Project administration, Methodology, Funding acquisition, Conceptualization. **Erik Smolders:** Writing – review & editing, Supervision, Methodology, Conceptualization.

Declaration of competing interest

The authors declare that they have no known competing financial interests or personal relationships that could have appeared to influence the work reported in this paper.

Data availability

Data will be made available on request.

Acknowledgment

This research has received funding from the European Union's Horizon 2020 research and innovation program under the Marie Sklodowska-Curie Grant Agreement No 857989.

The authors gratefully acknowledge the valuable assistance of the following people: Dr. C.R Cánovas and Dr. Raul Moreno Gonzalez from the Department of Earth Sciences, University of Huelva in Spain for aid in collecting acid mine water samples; Dr. Claudia Moens, Mr. Benoit Bergen, Ms. Kristin Coorevits and ICP-MS Team, Division of Soil and Water Management, KU Leuven for their enormous assistance in measuring ICP-MS samples; Dr. Charlotte Vermeiren, Dr. Ir. Alicia Van Ham-Meert, Dr. Claudia Moens, Ms. Jasnalien Ceulemans, Mr. Jesse Dekeyrel and LA-ICP-MS Team, Division of Soil and Water Management, KU Leuven for their immense assistance in measuring LA-ICP-MS samples; SOLEIL for having provided synchrotron radiation facilities under the project no. 99220057 at the LUCIA beamline; All the technicians of the Waste and Disposal Group, SCKCEN for their assistance in various ways.

Appendix A. Supplementary data

Supplementary data to this article can be found online at https://doi.org/10.1016/j.scitotenv.2024.174895.

References

Akinwekomi, V., Kefeni, K.K., Maree, J.P., Msagati, T.a.M., 2016. Integrated acid mine drainage treatment using Mg(OH) 2 or Mg(HCO3)2 and Ca(OH)2: implications for separate removal of metals and sulphate. Int. J. Miner. Process. 155, 83–90.

Ayora, C., Caraballo, M.A., Macias, F., Rotting, T.S., Carrera, J., Nieto, J.M., 2013. Acid mine drainage in the Iberian Pyrite Belt: 2. Lessons learned from recent passive remediation experiences. Environ. Sci. Pollut. Res. Int. 20 (11), 7837–7853.

Ayora, C., Macias, F., Torres, E., Lozano, A., Carrero, S., Nieto, J.M., Perez-Lopez, R., Fernandez-Martinez, A., Castillo-Michel, H., 2016. Recovery of rare earth elements and yttrium from passive-remediation systems of acid mine drainage. Environ. Sci. Technol. 50 (15), 8255–8262.

Ayora, C., Carrero, S., Bellés, J., Basallote, M.-D., Cánovas, C.R., Macías, F., 2021. Partition of rare earth elements between sulfate salts formed by the evaporation of acid mine drainage. Mine Water Environ. 41 (1), 42–57.

Bau, M., Schmidt, K., Pack, A., Bendel, V., Kraemer, D., 2018. The European shale: an improved data set for normalisation of rare earth element and yttrium concentrations in environmental and biological samples from Europe. Appl. Geochem. 90, 142–149.

Bigham, J.M., Schwertmann, U., Traina, S.J., Winland, R.L., Wolff, M., 1996. Schwertmannite and the chemical modeling of iron in acid sulfate waters. Geochim. Cosmochim. Acta 60 (12), 2111–2121.

Bortnikova, S., Gaskova, O., Yurkevich, N., Saeva, O., Abrosimova, N., 2020. Chemical treatment of highly toxic acid mine drainage at a gold mining site in southwestern Siberia, Russia. Minerals 10 (10).

Cánovas, C.R., Nieto, J.M., Macías, F., Basallote, M.D., Olías, M., Pérez-López, R., Ayora, C., 2020. Recovery of critical raw materials from acid mine drainage (AMD). In: Elvis Fosso-Kankeu, C.W., Burgess, Jo (Eds.), Recovery of Byproducts from Acid Mine Drainage Treatment. Wiley.

Cheong, Y.-W., Cho, D.-W., Yim, G.-J., Park, H.-S., Kim, S.-J., Lee, J.-H., 2022. Geochemical assessment of gypsum scale formation in the hydrated lime neutralization Facility of the Daedeok Mine, South Korea. Minerals 12 (5).

Costis, S., Mueller, K.K., Coudert, L., Neculita, C.M., Reynier, N., Blais, J.-F., 2021. Recovery potential of rare earth elements from mining and industrial residues: a review and cases studies. J. Geochem. Explor. 221.

Doyle, C.S., Traina, S.J., Ruppert, H., Kendelewicz, T., Rehr, J.J., Brown Jr., G.E., 1999. XANES studies at the Al K-edge of aluminium-rich surface phases in the soil environment. J. Synchrotron Radiat. 6 (Pt 3), 621–623.

Dutrizac, J.E., 2017. The behaviour of the rare earth elements during gypsum (CaSO4·2H2O) precipitation. Hydrometallurgy 174, 38–46.

Ferreira Da Silva, E., Bobos, I., Xavier Matos, J., Patinha, C., Reis, A.P., Cardoso Fonseca, E., 2009. Mineralogy and geochemistry of trace metals and REE in volcanic massive sulfide host rocks, stream sediments, stream waters and acid mine drainage from the Lousal mine area (Iberian Pyrite Belt, Portugal). Appl. Geochem. 24 (3), 383–401.

Harvey, D., 2000. Modern Analytical Chemistry, 1 ed. James M. Smith.

Hassas, B.V., Rezaee, M., Pisupati, S.V., 2020. Precipitation of rare earth elements from acid mine drainage by CO2 mineralization process. Chem. Eng. J. 399, 11.

Jackson, S.L., 2006. Research Methods and Statistic: A Critical Thinking Approach, *2nd ed.* Thomson and Wadsworth, Belmont, CA.

Kotte-Hewa, D.J., Durce, D., Salah, S., Ruiz Cánovas, C., Smolders, E., 2023. Remediation of acid mine drainage and immobilization of rare earth elements: comparison between natural and residual alkaline materials. Appl. Geochem. 158.

Lachaux, N., Cossu-Leguille, C., Poirier, L., Gross, E.M., Giamberini, L., 2022. Integrated environmental risk assessment of rare earth elements mixture on aquatic ecosystems. Front. Environ. Sci. 10.

León, R., Macías, F., Cánovas, C.R., Pérez-López, R., Ayora, C., Nieto, J.M., Olías, M., 2021. Mine waters as a secondary source of rare earth elements worldwide: the case of the Iberian Pyrite Belt. J. Geochem. Explor. 224.

Lin, J., Nilges, M.J., Wiens, E., Chen, N., Wang, S., Pan, Y., 2019. Mechanism of Gd3+ uptake in gypsum (CaSO4·2H2O): implications for EPR dating, REE recovery and REE behavior. Geochim. Cosmochim. Acta 258, 63–78.

London., T.G.S.O., *Rare Earth Elements: A briefing note by the Geological Society of London*. 2011.

Lozano, A., Fernandez-Martinez, A., Ayora, C., Di Tommaso, D., Poulain, A., Rovezzi, M., Marini, C., 2019a. Solid and aqueous speciation of yttrium in passive remediation Systems of Acid Mine Drainage. Environ. Sci. Technol. 53 (19), 11153–11161.

Lozano, A., Ayora, C., Fernández-Martínez, A., 2019b. Sorption of rare earth elements onto basaluminite: the role of sulfate and pH. Geochim. Cosmochim. Acta 258, 50–62.

Lozano, A., Ayora, C., Macías, F., León, R., Gimeno, M.J., Auqué, L., 2020a. Geochemical behavior of rare earth elements in acid drainages: modeling achievements and limitations. J. Geochem. Explor. 216.

Lozano, A., Ayora, C., Fernández-Martínez, A., 2020b. Sorption of rare earth elements on schwertmannite and their mobility in acid mine drainage treatments. Appl. Geochem. 113.

Lozano, A., Ayora, C., Fernandez-Martinez, A., 2020c. Sorption of rare earth elements on schwertmannite and their mobility in acid mine drainage treatments. Appl. Geochem. 113, 104499.

Ma, X., Gomez, M.A., Yuan, Z., Bi, R., Zhang, J., Wang, S., Yao, S., Kersten, M., Jia, Y., 2020. Incorporation of trace metals Cu, Zn, and Cd into gypsum: Implication on their mobility and fate in natural and anthropogenic environments. Chem. Geol. 541.

Migaszewski, Z.M., Gałuszka, A., 2014. The characteristics, occurrence, and geochemical behavior of rare earth elements in the environment: a review. Crit. Rev. Environ. Sci. Technol. 45 (5), 429–471.

Naidu, G., Ryu, S., Thiruvenkatachari, R., Choi, Y., Jeong, S., Vigneswaran, S., 2019. A critical review on remediation, reuse, and resource recovery from acid mine drainage. Environ. Pollut. 247, 1110–1124.

Noack, C.W., Dzombak, D.A., Karamalidis, A.K., 2014. Rare earth element distributions and trends in natural waters with a focus on groundwater. Environ. Sci. Technol. 48 (8), 4317–4326.

Project, T.M. *CaH_4SO_6 mp-23690*. 2022 [cited 2022 2022/06/22]; Available from: https://next-gen.materialsproject.org/materials/mp-23690/#contributed_data.

Prudencio, M.I., Valente, T., Marques, R., Sequeira Braga, M.A., Pamplona, J., 2015. Geochemistry of rare earth elements in a passive treatment system built for acid mine drainage remediation. Chemosphere 138, 691–700.

Rotting, T.S., Thomas, R.C., Ayora, C., Carrera, J., 2008. Passive treatment of acid mine drainage with high metal concentrations using dispersed alkaline substrate. J. Environ. Qual. 37 (5), 1741–1751.

Royer-Lavallee, A., Neculita, C.M., Coudert, L., 2020. Removal and potential recovery of rare earth elements from mine water. J. Ind. Eng. Chem. 89, 47–57.

Ruehl, M.D., Hiibel, S.R., 2020. Evaluation of organic carbon and microbial inoculum for bioremediation of acid mine drainage. Miner. Eng. 157.

Sadri, F., Kim, R., Yang, Z., Ghahreman, A., 2018. The effect of calcium sulfate crystallization and the crystal modification on aqueous REE stability in Ca saturated REE-Ca-SO4-H2O systems. Hydrometallurgy 182, 82–96.

Sadri, F., Kim, R., Ghahreman, A., 2019. Substitution of calcium with Ce, Nd, Er, and Tb in the structure of microcrystals of calcium sulfates with controlled hydration water: a proposed mechanism. Cryst. Growth Des. 19 (5), 2621–2631.

Sanchez, M., Sabio, L., Galvez, N., Capdevila, M., Dominguez-Vera, J.M., 2017. Iron chemistry at the service of life. IUBMB Life 69 (6), 382–388.

Sánchez-España, J., Yusta, I., Diez-Ercilla, M., 2011. Schwertmannite and hydrobasaluminite: a re-evaluation of their solubility and control on the iron and aluminium concentration in acidic pit lakes. Appl. Geochem. 26 (9–10), 1752–1774.

Wang, Y., Noble, A., Vass, C., Ziemkiewicz, P., 2021. Speciation of rare earth elements in acid mine drainage precipitates by sequential extraction. Miner. Eng. 168.

Zänker, H., Richter, W., Hüttig, G., 2003. Scavenging and immobilization of trace contaminants by colloids in the waters of abandoned ore mines. Colloids Surf. A Physicochem. Eng. Asp. 217 (1–3), 21–31.